Influence of Nickel on the Microstructure, Mechanical Properties, and Corrosion Resistance of Laser-Welded Super-Duplex Stainless Steel

E.J. da Cruz Junior, J. Gallego, A.G. Settimi, C. Gennari, A. Zambon, and V.A. Ventrella

Super-duplex stainless steel (SDSS) exhibits an austenite-ferrite dual-phase structure, which promotes many benefits upon single-phase grades, such as high mechanical strength and corrosion resistance. Welding process results in an unbalanced microstructure, with large amount of ferrite, which compromise SDSS's properties. This paper investigates the effect of using electrolytic nickel foils as an addition metal on UNS S32750 SDSS Nd:YAG pulsed laser welding, through the evaluation of the microstructure, hardness, tensile strength, and corrosion resistance of the weld bead. Six conditions were investigated: autogenous welding and with addition of nickel, varying the thickness of nickel foil added. Microstructural analysis reveals an increase in volume fraction of austenite for the conditions with addition of nickel. Using a 30 μm thick nickel foil, approximately equal amount of austenite and ferrite was obtained in the weld bead. The higher microhardness was obtained for the autogenous welding, 400 HV and decreased with the addition of nickel. The tensile strength decreased 4% in the experimental conditions with high nickel addition. The corrosion resistances were the same for all the conditions with addition on nickel, regardless of the nickel foil thickness added, but it compared to autogenous welding the CPT's increased approximately 14 °C.

1. Introduction

Super-duplex stainless steels (SDSS) are characterized by a dual-phase microstructure consisting of approximately equal volume fractions of FCC austenite and BCC ferrite, which promotes an optimal combination of mechanical strength and corrosion resistance (Ref 1)

. These alloys are about twice as strong as austenitic steels (Ref 2). Due to their high properties, these steels have a wide range of applications in the chemical, oil and gas, petrochemical, pulp and paper, offshore and marine industries (Ref 3).

It is not easy to select the SDSS welding process for the proportion of austenite and ferrite should not be affect during the welding. The welding process frequently results in an unbalanced microstructure, with a large amount of ferrite, which compromises SDSS's properties like local pitting corrosion resistance and toughness (Ref 4). Another difficulty

is the fact that depending of the welding process and parameters, in the temperature range between 700 and 950 °C detrimental secondary phases can precipitate. These phases will affect the mechanical properties and corrosion resistance of the SDSS (Ref 5). Welding process with high energy input can lead to weld bead deformation, large heat-affected zone (HAZ), and poor corrosion resistance (Ref 6). Arun et al. (Ref 7) have stated that to obtain the optimal phase balance in the fusion zone is a hard challenge.

In DSS welding austenite is formed from solid-state ferrite. Welding conditions with low cooling rates favor the growth of ferritic grains in the heat-affected zone (HAZ) and the formation of nitrides and carbides. High cooling rates favor a higher amount of ferrite, not having the time required for austenite formation (Ref 3).

The Nd:YAG pulsed laser welding process offers some advantages over conventional processes, namely accuracy, complex shape welding, short cycle time, and low heat input (Ref 3). Ventrella et al. (Ref 8) concluded that Nd:YAG pulsed laser is the best welding process when precise heat input control and lower heat-affected zone are required. Low heat input and high cooling rates, which are typical of the process, promote the formation of BCC ferrite which results in an undesired microstructure for most applications (Ref 9). To obtain a balanced microstructure, a post-weld heat treatment and/or the addition of strong austenite-promoting elements to the welding pool, such as nickel, might prove useful (Ref 10). Other alternatives such as dissimilar welding (Ref 10), heat input control (Ref 11) and use of shielding gas rich in austenite-promoting elements (Ref 12) are reported in the literature.

Many studies related to the effect of addition of γ (FCC) stabilizers on the phase balance in the welding process could be found in literature, however, related to the Nd:YAG pulsed laser welding no remarkable results have been yet obtained. Muthupandi et al. (Ref 13) studied the influence of nickel

E.J. da Cruz Junior, Federal Institute of São Paulo, Avenue Jerônimo Figueira da Costa 3014, Votuporanga, SP 15503-110, Brazil; **J. Gallego** and **V.A. Ventrella**, Department of Mechanical Engineering, Sao Paulo State University, Avenue Brasil 56, Ilha Solteira, SP 15385-000, Brazil; **A.G. Settimi** and **C. Gennari**, Department of Industrial Engineering, University of Padua, Via Gradenigo, 6/a, 35131 Padova, Italy; **A. Zambon**, Department of Management and Engineering, University of Padua, Stradella S. Nicola, 3, 36100 Vicenza, Italy. Contact e-mail: dacruz.eli@ifsp.edu.br.

and nitrogen addition on the microstructure and mechanical properties of power laser beam processed DSS weld metals. Migiakis and Papadimitriou (Ref 14) performed a similar study but applied to plasma welding. Pilhagen and Sandström (Ref 15) have investigated the role of nickel on the toughness of lean DSS weld metal prepared by submerged arc welding (SAW). Tahaei et al. (Ref 16) studied the effect of nickel and post-weld heat treatment applied to gas tungsten arc welding (GTAW). Zhang et al. (Ref 17) also have worked with GTAW but have given emphasis to nitrogen as the shielding gas. Related to the Nd:YAG pulsed laser process it's hard to find results in literature; da Cruz Junior et al. (Ref 18) reported some preliminary results related to Nd:YAG pulsed laser welding but they studied only two conditions and did not address corrosion resistance and mechanical properties.

The Nd:YAG pulsed laser welding characteristics, e.g., low heat input, short cycle time, high cooling rates, make the addition of alloying elements, whether as welding filaments or shielding gas, rather difficult to achieve, if homogeneity in the resulting local composition and/or microstructure of the weld bead is seeked. Finding a way to add austenite-promoting is very important to make this laser welding process applicable to duplex stainless steels.

An increase in the utilization of materials with high mechanical properties and corrosion resistance, like SDSS, leads to the need of more efficient welding processes. Due to the importance of the phase balance in relation to the properties of SDSS and its applications and considering the role of nickel as austenite-promoting on SDSS welding, the objective of this work is to investigate the effect of using electrolytic nickel foils as an addition metal on UNS S32750 SDSS Nd:YAG pulsed laser welding. This study evaluated the microstructure, hardness, tensile strength and corrosion resistance of weld beads using nickel foils of different thickness.

2. Materials and Methods

Sheets 1.5 mm thick of UNS S32750 SDSS were used as base metal. The chemical composition (informed by the supplier) is reported in Table 1 and the microstructure is shown in Fig. 1(a).

Electrolytic nickel thin foils with different thickness (Table 2) were inserted between the two pieces of UNS S32750 that were to be welded as displayed in Fig. 1(b), providing nickel enrichment in the weld metal. The nickel foils were obtained from an electrolytic nickel bar. Using a wire electrical discharge machining, strips were cut and subsequently sanded to the desired thickness.

A Nd:YAG pulsed laser facility model UW-150A, with a 150 W maximum power, beam spot diameter of 0.2 mm was employed. Six conditions were evaluated, keeping the same welding parameters and varying the thickness of nickel foil added. The welding parameters were the same for all the

samples once the objective of the work was to evaluate the effect of nickel addition. Single-pass welding was applied. After exploratory tests, the welding parameters were selected to achieve a regular surface, without porosity, and a weld pool depth higher than 50 % of the sheet thickness. The laser beam, keyhole mode, with pulse energy set at 10 J was focused on the sample surface. Table 2 summarizes the welding parameters and the thickness of nickel foil used in the experiments.

The critical pitting temperature (CPT) was used to evaluate the corrosion resistance, according to ASTM G150-18 standard (Ref 19). Three samples for each condition were tested. CPT test was chosen to correlate the microstructure modifications to the corrosion properties (Ref 20). The samples were varnished with a thermal-resistant varnish letting exposed an area of 1 cm^2. A potentiostat (model AMEL 7060) was used to perform the test and to record the current density which was continuously measured and verified with reference to a standard electrode. To this end, two cells containing aqueous solution of NaCl (1 M), electrically connected by a salt bridge, were used to immerse the working electrode, the counter electrode and the reference electrode. In particular, the standard calomel electrode (SCE) was immersed in the first cell and maintained at room temperature. The platinum counter electrode and the sample
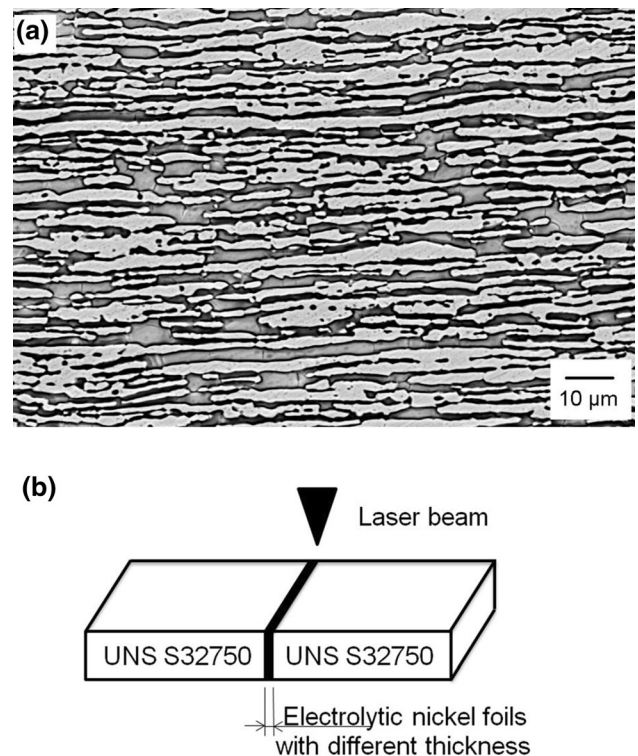

Fig. 1 (a) SEM (secondary electron detector, EHT = 20.00 kV, WD = 12.5 mm) micrograph of UNS S32750 (b) Schematic diagram of the butt weld joint arrangement

Table 1 Chemical composition of UNS S32750 (wt.%)

UNS S32750	C	Si	Mn	P	S	Cr	Mo	Ni	Cu	N
	0.018	0.29	0.63	0.02	< 0.0003	25.61	3.84	6.97	0.15	0.27

Table 2 Welding parameters and thickness of the nickel thin foils for the samples

Samples denomination	Nickel foil thickness	Welding parameters (same for all the conditions)
AW	No nickel foil	Peak power: 2.0 kW
Ni30	30 μm	Pulse duration: 5 ms
Ni40	40 μm	Frequency: 9 Hz
Ni50	50 μm	Welding speed: 1 mm/s
Ni60	60 μm	Shielding gas: pure argon (Ar)
Ni70	70 μm	Flow rate: 20 l/min

(working electrode) were immersed in the second cell where the temperature was raised at a rate of 1 ºC/min starting from 0 ºC until the temperature that the current density reached 100 μA/cm^2. CPT is defined when the current density reaches 100 μA/cm^2 and remains above this level for a minimum of 60 s. Higher temperatures indicate better pitting corrosion resistance (Ref 19). Potential was set to 700 mV vs SCE and kept constant, as defined by ASTM G150-18 standard. The pitting locations were observed by stereomicroscopy Zeiss Stereoscan Stemi C2000.

After the welding process, the samples were cut transversal with respect to the weld direction for the metallographic analysis. The samples were embedded in cold-curing transparent epoxy resin using a silicone mold. The sanding of the samples occurred manually, alternating the position by 90° in each sanding change. For the polishing, alumina suspension was used. In order to reveal the microstructure, Beraha's reagent was used. The austenite/ferrite volume fraction was calculated using SEM micrographs (Carl Zeiss EVO LS15) and ImageJ free software. For each sample, ten SEM micrographs were analyzed. The micrographs were binarized, austenite resulting light, and ferrite dark. Comparing the areas relating to austenite and ferrite in the micrograph the austenite/ferrite ratio were calculated.

The Vickers microhardness was measured across the entire width of the weldments, perpendicular to welding direction, using a Dynamic Ultra Micro Hardness Tester Shimadzu DUH 211S. Three samples for each condition were tested. The measurements were carried out at intervals of 0.05 mm. A standard test load of 10 gf was applied for a dwell time of 15 s using a square pyramidal diamond indenter.

To evaluate the weldments for tensile properties, the samples were dimensioned as per ASTM E8/E8M-16ae1 standards (Ref 21), being tested on a universal testing machine EMIC DL 30.000 at room temperature. Tensile properties were estimated by setting the cross-head velocity to 2 mm/min so as to introduce a lower strain rate of 3.3 x 10^{-4} s^{-1}. Three trials on each condition were conducted to check the reproducibility of the results. The fracture surfaces of the samples after tensile testing were examined via scanning electron microscopy to investigate the mode of fracture.

3. Results and Discussion

3.1 Microstructure

The microstructures of the weld bead for all the samples are shown in Fig. 2. Austenite is light and ferrite is dark. It is clear that nickel acted modifying both the amount of austenite and its morphology. The autogenous welding specimen (AW) has presented a strongly unbalanced microstructure (Fig. 2a), containing a large amount of polygonal ferrite grains with austenite decorating its boundaries, typical result of Nd:YAG pulsed laser welding (Ref 18). Additions of nickel have resulted in an effective increase in the austenite amount in the SDSS weld metal. Ni30 sample (Fig. 2b) resulted in well-balanced ferrite-austenite microstructure, where austenite developed at the prior ferrite grain boundaries (allotriomorphic) and inside them (idiomorphic) too. Higher amounts of austenite have been found with increasing nickel foil thickness in the case of the samples Ni40 (Fig 2c), Ni50 (Fig 2d), Ni60 (Fig 2e), and Ni70 (Fig. 2f), the latest being mainly austenitic due to massive concentration of γ-stabilizing elements.

During DSS welding, the formation of austenite derives from a diffusional solid-state transformation. The heat input and the cooling rates experienced by the bead during the thermal cycle will affect austenite formation. Under high cooling rates, peculiar to the pulsed laser parameters set, there is not enough time for completing austenite formation, which results in a predominantly ferritic microstructure, as found on the AW sample (Ref 22). SEM analyses have identified different austenite morphologies depending on nickel foil thickness. Allotriomorphic austenite and Widmanstätten side-plates have been identified growing into the ferrite grains starting from the grain boundaries while idiomorphic austenite grains form inside the ferritic grains. Allotriomorphic and Widmanstätten austenite form at higher temperatures, while idiomorphic austenite forms at lower temperatures and at higher cooling rates (Ref 23). The great amount of idiomorphic austenite in the Ni30 sample resulted from the thermal cycle (high cooling rate) associated with the austenite formation potential of nickel.

In the Ni30 sample, the microstructure was very homogeneous along the weld bead, and a well-balanced microstructure consisting of equal amount of austenite and ferrite was achieved. Phase balance in DSSs is very important to obtain optimum combination of mechanical properties and corrosion resistance (Ref 4)). Increased nickel addition resulted in higher volume fraction of austenite which deteriorates corrosion and mechanical properties of the weld bead.

The quantitative effect of nickel on the laser welding process can be observed in Table 3, which shows the mean volume fraction of austenite and ferrite for the base metal and for all the samples. As mentioned the results were obtained by image analysis, for each sample, ten SEM micrographs were analyzed.

The volume fractions showed that the Ni30 sample achieved a balanced ferrite/austenite microstructure. Comparing the AW and Ni30 sample, the addition of nickel increased the proportion of austenite from approximately 8% (AW) to 52% (Ni30). This effect was a direct consequence of the addition of
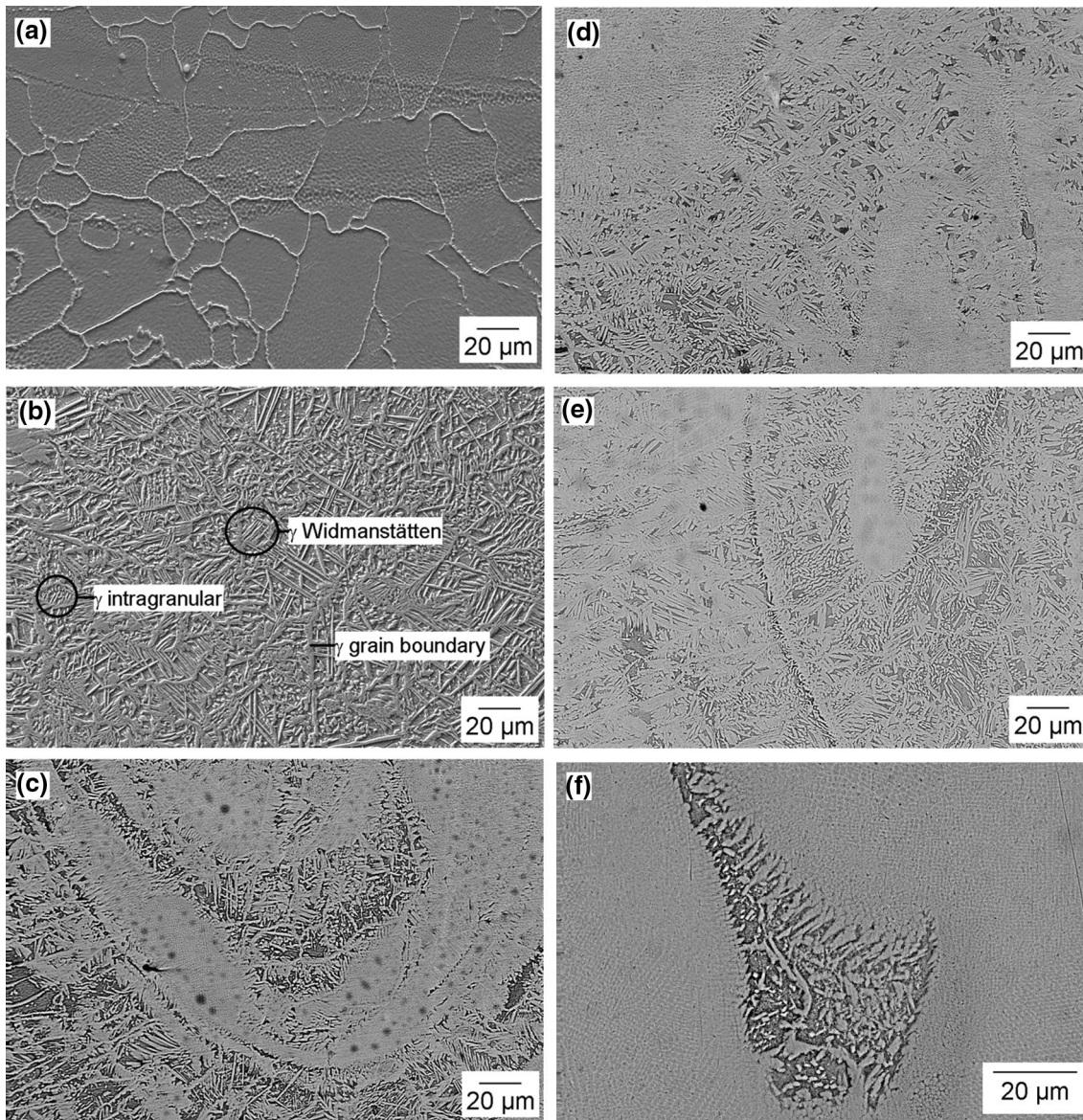
Fig. 2 Micrographs (SEM–secondary electron detector, EHT = 20.00 kV, WD = 9.5 mm) of weld bead for (a) AW, (b) Ni30, (c) Ni40, (d) Ni50, (e) Ni60, and (f) Ni70. Austenite is light and ferrite is dark. Beraha's etching

Table 3 Phase balance for all the samples (v/v)

	Phase proportion		
	Ferrite %	**Austenite %**	**SD**
Base metal	50.2	49.8	0.4
AW	92.4	7.6	0.5
Ni30	48.2	51.8	0.4
Ni40	30.2	69.8	0.7
Ni50	21.1	78.9	1.2
Ni60	18.7	81.3	1.0
Ni70	4.6	95.4	1.2

nickel considering that the welding parameters were kept constant.

The AW sample presented a ferrite volume fraction of approximately 93%, while the Ni70 sample presented an austenite volumetric fraction of approximately 95%. Higher amount of austenite will increase the corrosion resistance of the weld bead, but it decreases mechanical properties, e.g., microhardness and tensile strength, due to lack of ferrite.

The microstructures in the transition region between the base metal and weld bead for all the samples are shown in Fig. 3. For all the samples with nickel addition, although the amount of austenite in the fusion zone is greater than 50%, the amount of ferrite was higher than that of austenite in the heat-affected zone (HAZ). Even for the Ni30 sample, although the microstructure in the fusion zone is balanced, the HAZ presented an unbalanced microstructure with a higher amount of ferrite.

The temperature reached in the HAZ is not high enough to melt the material, but since phase balance depends on the temperature and cooling rate, it modifies the amount of austenite and ferrite. In the HAZ, austenite volume fraction is slightly lower compared to the weld bead, which occurs
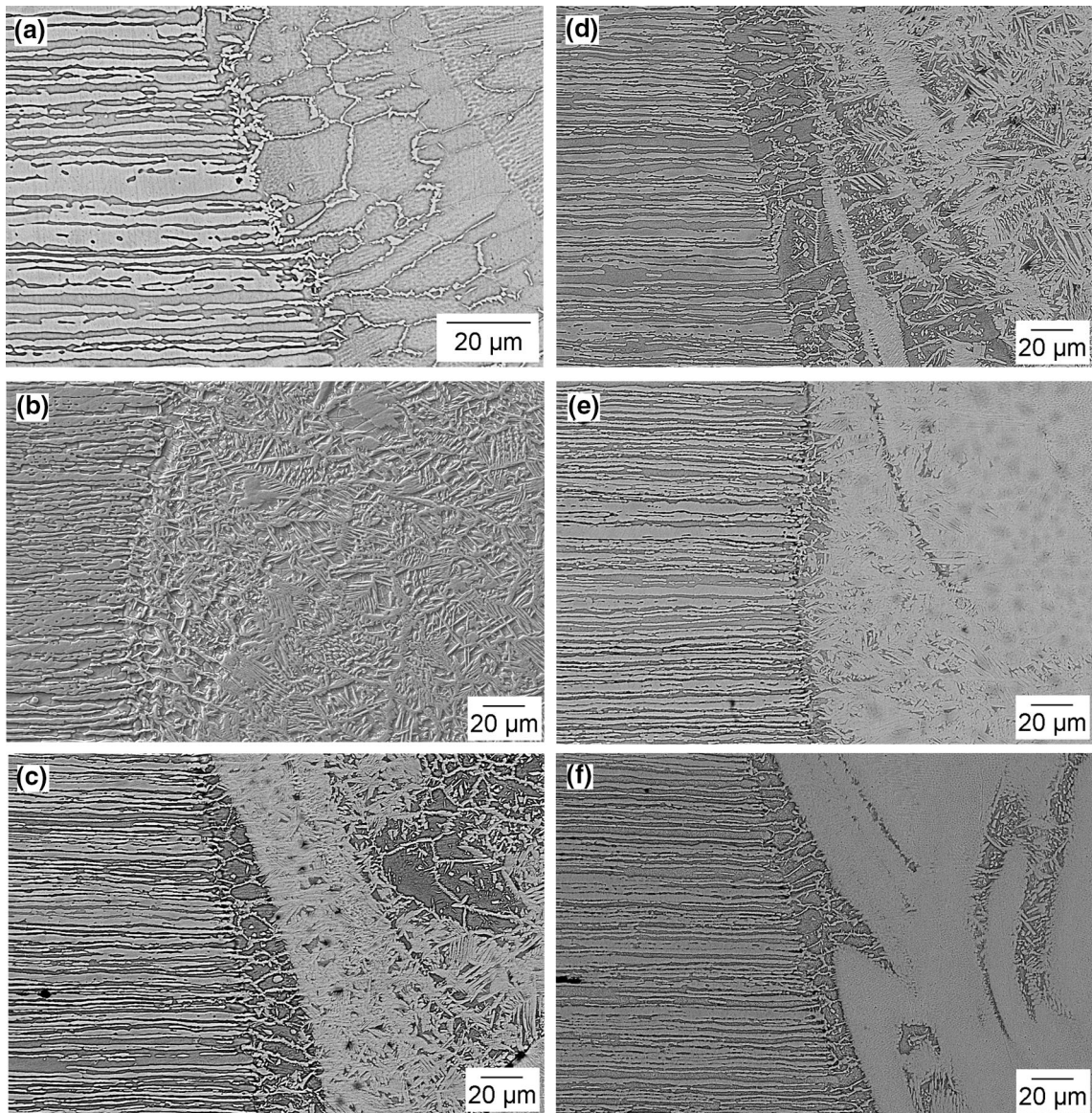
Fig. 3 Micrographs (SEM–secondary electron detector, EHT = 20.00 kV, WD = 9.5 mm) of transition between base metal and weld bead for (a) AW, (b) Ni30, (c) Ni40, (d) Ni50, (e) Ni60, and (f) Ni70. Austenite is light and ferrite is dark. Beraha's etching

because the cooling rate is higher in this region. Since austenite formation occurs through a diffusional solid-state transformation, high cooling rates do not allow enough time for austenite to form. Post-weld heat treatment could be an option to improve the phase balance on the HAZ. Unbalanced microstructure will affect both corrosion and mechanical properties resulting in a weaker region in correspondence of the HAZ.

The duplex stainless steels show a rather complex second-phase precipitation and phase transformation behavior because of its high amount of alloying elements. In some welding processes like submerged arc welding (SAW), gas tungsten arc welding (GTAW) or laser-beam welding (LBW), which may be followed by an isothermal heat treatment (Ref 24-26), secondary phases can precipitate in a temperature range between 700 ºC and 950 ºC (Ref 27). High ferrite contents can lead to intense chromium nitride precipitation, caused by low nitrogen solubility in ferrite. In addition, chromium nitride particles are also believed to be nucleation sites for pitting (Ref 28). The low

heat input associated with the high cooling rate of Nd:YAG pulsed laser welding does not favor the formation of these phases.

To confirm the absence of secondary phases, the samples were carefully analyzed by SEM with backscattered electron detector. In this case, the samples were not etched. Secondary phases should appear as a lighter spots located between ferrite grains and at austenite–ferrite phase boundaries, while chromium nitrides should appear as dark necklaces at ferrite/ferrite grain boundaries. No secondary phase was detected. Figure 4 shows the micrograph for Ni30 sample, which represents the combination of added nickel quantity and thermal sequence that afforded to achieve the phase balance.

3.2 Microhardness

The microhardness profile for all conditions is shown in Fig. 5. The base metal mean microhardness was 307 ± 4 HV. As expected, a decrease in hardness is observed as the austenite

volume fraction increases. For Ni50, Ni60, and Ni70 samples, the microhardness values are similar due to the resulting microstructure is mainly austenitic, with some minor biphasic regions (austenite and ferrite).

The mean microhardness for the weld bead for each condition is shown in Table 4. The mean value of microhardness in the fusion zone for the AW sample was 400 ± 2 HV, while for the Ni30 sample it was 365 ± 9 HV. Since AW sample presented a predominantly ferritic microstructure, the microhardness in the fusion zone was higher. Although for Ni30 sample, the phase balance is close to that of the base material, and the microhardness was approximately 20% higher. The formation of intragranular (idiomorphic) austenite
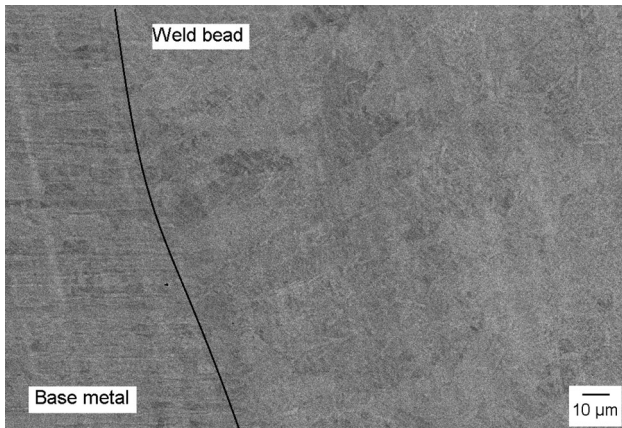

Fig. 4 SEM (backscattered electron) micrograph for Ni30 condition. Dark line from top to bottom of image was added to point out the boundary between the two zones shown on the image
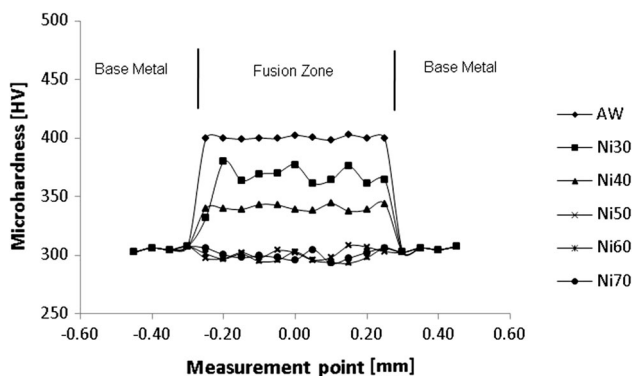

Fig. 5 Microhardness profile

Table 4 Microhardness

Sample denomination	Fusion zone, HV
AW	400 ± 2
Ni30	365 ± 9
Ni40	342±3
Ni50	303 ± 5
Ni60	298 ± 3
Ni70	298 ± 4

together with the high cooling rate introduced strain hardening effect in the microstructure, increasing the hardness as previously observed by Tahaei et al. (Ref 16).

The nickel content is a key factor to achieve satisfactory toughness values in DSS welds since a proper nickel amount can increase the austenite content and, on the other hand, raise the toughness of ferrite (Ref 15). Due to the increase in the austenite content and the decrease in hardness observed, it can be envisaged that the Ni30 sample could provide a weld bead with higher toughness in comparison with the AW one.

3.3 Tensile Strength

Specimens for the tensile tests are depicted in Fig. 6 and the results of the tensile tests are showed in Table 5. For AW, Ni30 and Ni40 samples, the ultimate tensile strength (UTS) was the same of the base metal since fracture occurred in this region (as presented in Fig. 6). For these samples, the weld bead presented higher resistance than the base metal. For Ni50, Ni60, and Ni70 samples, there were moderate reductions in the tensile strength, and the fractures occurred in the weld bead. As already mentioned, the weld bead hardness values for these conditions were slightly lower than that of the base metal, which properly correlates with the observed slight decrease in tensile strength.

Comparing the tensile strength of the Ni70 sample (which showed the lowest tensile strength) and the base metal, it was observed that the influence of the nickel on the tensile strength was not significant, once there was only a drop of 4% in resistance. Saravanan et. al. (Ref 29) in their study on the effect of heat input on microstructure and mechanical properties in DSS laser welding also observed a small decrease in tensile due to the higher austenite volume fraction.

The elongation decreased for the samples Ni50, Ni60, and Ni70, indicating loss in ductility. As the fractures occurred in the weld bead, the fracture mechanism was different in relation to the samples where the fracture occurred in the base metal. The fractographs presented in Fig. 7 indicate this change in the fracture mechanism.

Figure 7 shows the fractograph of the base metal and of the Ni50 sample (once that Ni50, Ni60, and Ni70 have the same fracture behavior). The fracture surface of the base metal (Fig. 7a) is cleavage free with an evident necking area (Fig. 7c), typical of a ductile fracture. In the Ni50 sample (Fig. 7b), it is possible to observe dimples and also some cleavage marks, while necking (Fig 7d) is very small indicating little deformation before fracture.
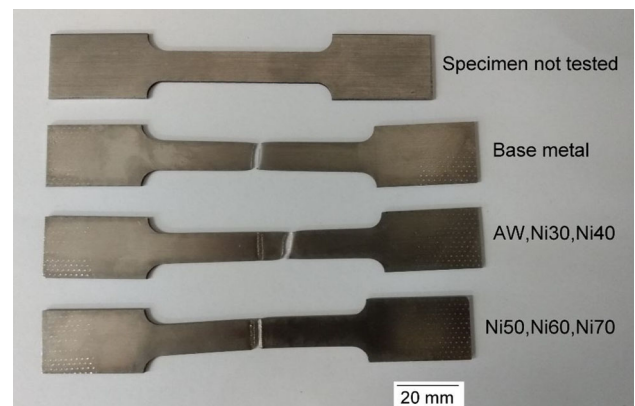

Fig. 6 Tensile test specimens

Table 5 Results of tensile tests

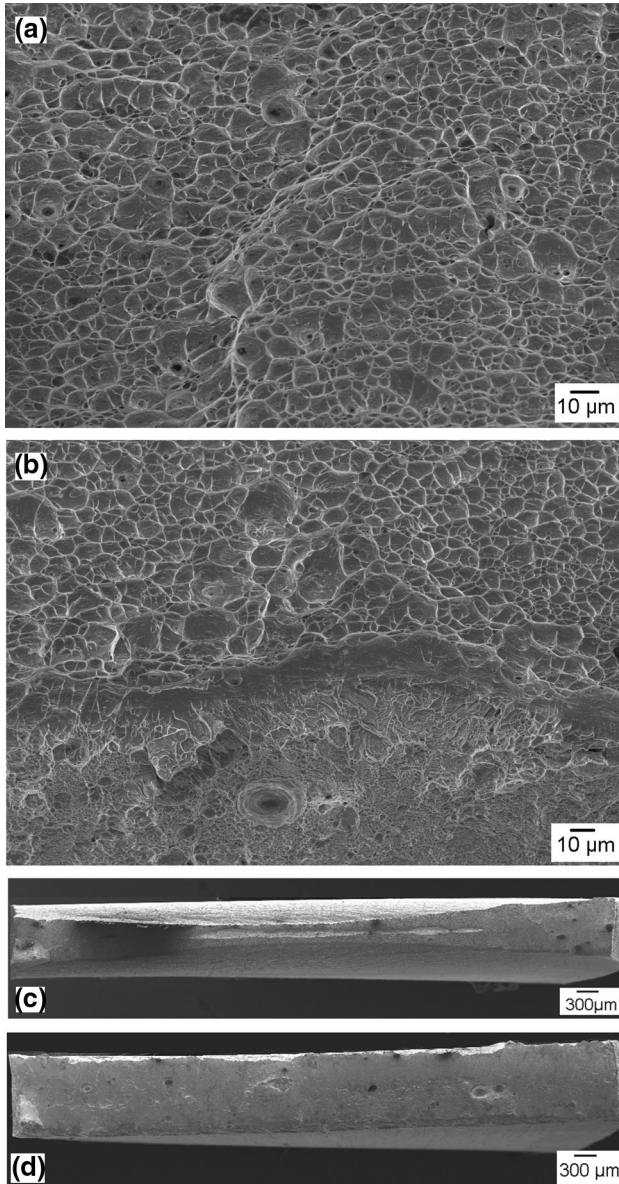| Condition	Ultimate tensile strength, MPa	Elongation, %	Location of fracture
Base metal	845 ± 9	26 ± 1	Base metal
AW	845 ± 9	26 ± 1	Base metal
Ni30	845 ± 8	26 ± 1	Base metal
Ni40	845 ± 8	26 ± 1	Base metal
Ni50	840 ± 11	20 ± 1	Weld bead
Ni60	822 ± 10	21 ± 1	Weld bead
Ni70	812 ± 11	18 ± 1	Weld bead

Fig. 7 SEM fractures of samples for (a) base metal, (b) Ni50, (c) base metal, and (d) Ni50

3.4 Critical Pitting Temperature (CPT)

The results of CPT tests are presented in Fig. 8 and Table 6.

The AW sample showed the lowest CPT (36 °C), and a reduction of approximately 48 °C compared to the base metal
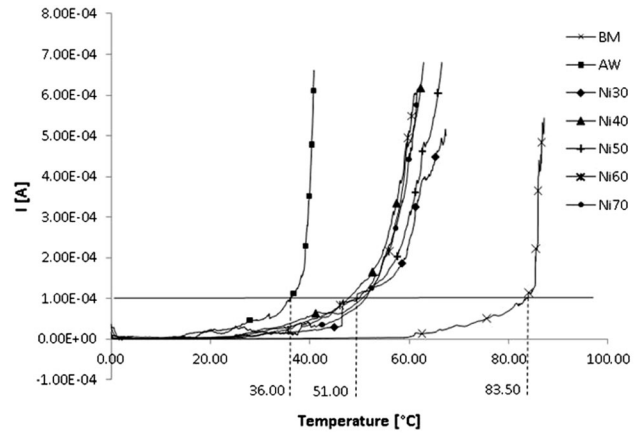

Fig. 8 CPT curves

Table 6 CPT results

	CPT, °C
Base metal	83.5 ± 1.2
AW	36.0 ± 1.5
Ni30	49.5 ± 1.1
Ni40	49.0 ± 1.3
Ni50	50.5 ± 1.2
Ni60	50.0 ± 1.0
Ni70	51.0 ± 1.2

(83.5 °C) because of the highest ferrite volume fraction. Austenite content seems to be in direct relation with the corrosion resistance, hence the lower CPT of the AW sample.

The CPTs for the samples with nickel addition were approximately the same regardless of the amount of nickel added. The higher the amount of austenite, the greater the resistance of the weld bead to corrosion (Ref 17, 20). However, in all the samples with addition of nickel the pitting occurred outside the weld bead, i.e., in the HAZ, while the AW samples showed the pitting occurring in the weld bead. Figure 9 shows the location of pitting for all the samples.

As observed in Fig. 3, in all samples with nickel addition, although in the fusion zone, the volume fraction of austenite is higher than 50%, the HAZ presents an unbalanced microstructure with greater amount of ferrite. This predominance of ferrite negatively affected the corrosion resistance of the HAZ, being the region where pitting occurred.

Although the samples with addition of nickel presented CPT's lower in comparison with the base metal, when
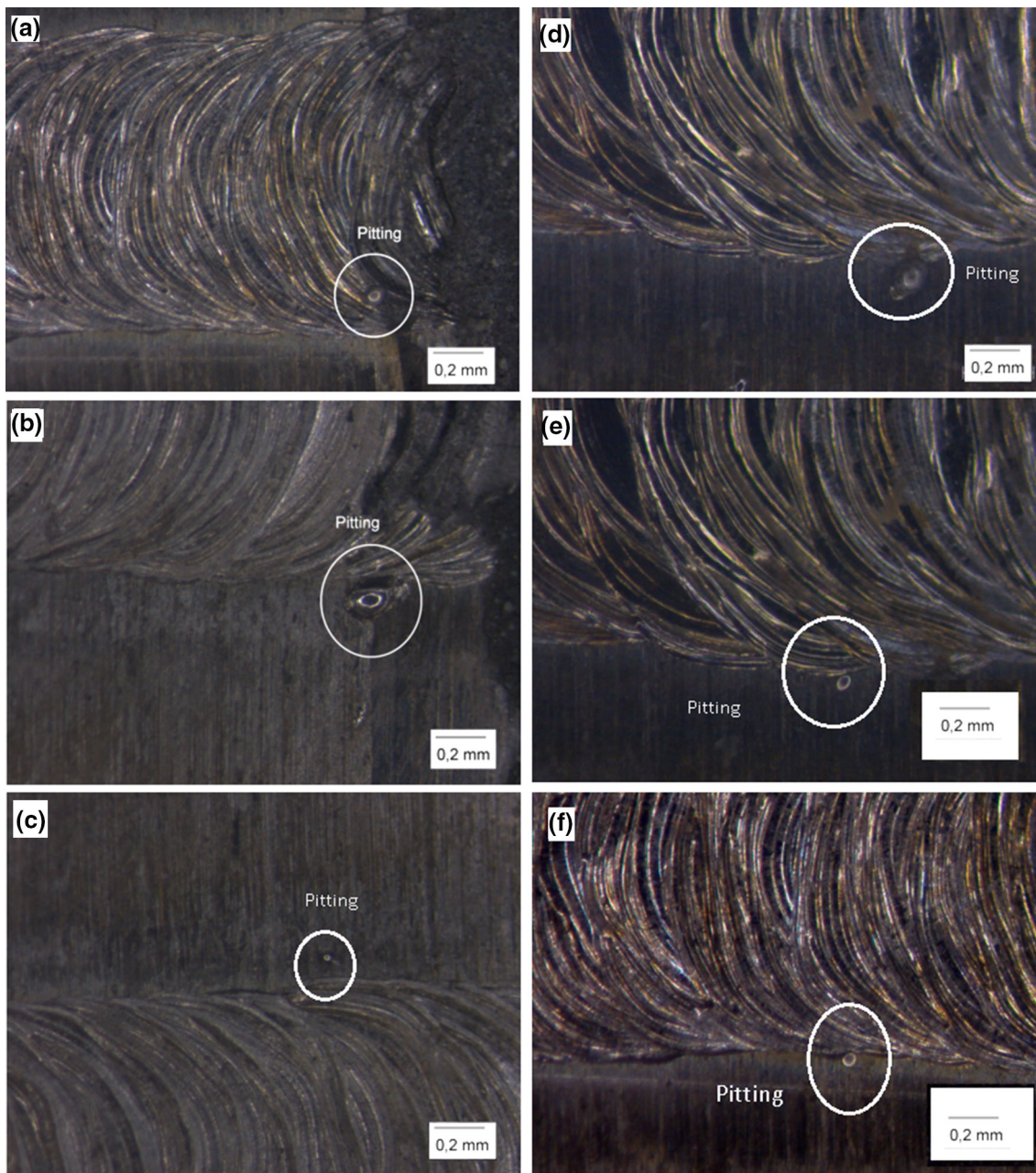
Fig. 9 Pits location after CPT tests for (a) AW and (b) Ni30 (c) Ni40, (d) Ni50, (e) Ni60, and (f) Ni70

compared to the CPT of the AW sample, they presented an increase in approximately 14 °C, which represents a significant increase in corrosion resistance.

4. Conclusions

The following conclusions could be drawn:

1. Nickel addition affected the formation of austenite both quantitatively and qualitatively, modifying its morphology and volume fraction.
2. The addition of nickel has affected the microstructure, mechanical properties, and corrosion resistance. Using a 30 μm thick nickel foil (Ni30) was the best condition.

Ni30 sample achieved the phase balance; consequently, good mechanical strength and corrosion resistance were obtained.
3. Compared to autogenous welding, the welds performed with nickel addition showed a higher corrosion resistance in terms of increase in CPT's. The CPT's for the different nickel addition examined were approximately the same regardless the amount of nickel added. For the AW sample, the pitting occurred on the weld bead and for for all the samples with addition of nickel it occurred outside the weld bead, namely in the HAZ, likely because this region presents an unbalanced microstructure with higher amount of ferrite.
4. For the Ni30 sample, although the volume fraction of austenite in the fusion zone was close to that of the base

metal, the hardness was higher, since the morphology and arrangement of the austenite along the fusion zone affected the hardness of the region. On the other hand, hardness decreased with further increase in nickel added.

5. For the samples Ni30 and Ni40, the tensile strength was equal to that of the base metal; the fracture was ductile and occurred out of the welded region. The Ni50, Ni60, and Ni70 samples presented a slight decrease in tensile strength. The fracture was brittle and occurred on the weld bead.

Acknowlegedgments

References

1. Z. Zhang, H. Zhao, H. Zhang, J. Hu and J. Jin, Microstructure Evolution and Pitting Corrosion Behavior of UNS S32750 Super Duplex Stainless Steel Welds After Short-Time Heat Treatment, *Corros. Sci.*, 2017, **121**, p 22–31

2. K. Devendranath Ramkumar, G. Thiruvengatam, S.P. Sudharsan, D. Mishra and N. Arivazhagan, Characterization of Weld Strength and Impact Toughness in the Multi-pass Welding of Super-Duplex Stainless Steel UNS 32750, *Mater. Des.*, 2014, **60**, p 125–135

3. S. Saravan, K. Raghukandan and N. Sivagurumanikandan, Pulsed Nd:YAG Laser Welding and Subsequent Post-Weld Heat Treatment on Super Duplex Stainless Steel, *J. Manuf. Process.*, 2017, **25**, p 284–289

4. H. Tan, Z. Wang, Y. Jianga, Y. Yang, B. Deng, H. Song and J. Li, Influence of Welding Thermal Cycles on Microstructure and Corrosion Resistance of 2304 Duplex Stainless steels, *Corros. Sci.*, 2012, **55**, p 368–377

5. L. Pezato, M. Lago, K. Brunelli, M. Breda and I. Calliari, Effect of the Heat Treatment on the Corrosion Resistance of Duplex Stainless Steel, *J. Mater. Eng. Perform.*, 2018, **27**, p 3859–3868

6. L. Mei, D. Yan, S. Xie, Z. Lei and X. Ge, Effects of Cr_2O_3 Active Agent on the Weld Process Dynamic Behavior and Joint Comprehensive Properties of Fiber Laser Welded Stainless Steel Thick Plate, *Opt. Laser Eng.*, 2020, **128**, p 106027

7. D. Arun, K. Devendranath Ramkumar and R. Vimala, Multi-pass arc Welding Techniques of 12 mm Thick Super-Duplex Stainless Steel, *J. Mater. Process. Technol.*, 2019, **271**, p 123–146

8. V.A. Ventrella, J.R. Berreta and W. de Rossi, Pulsed Nd:YAG Laser Seam Welding of AISI 316L Stainless Steel Thin Foils, *J. Mater. Process. Technol.*, 2010, **210**, p 1838–1843

9. Y. Hu, Y. Shi, X. Shen and Z. Wang, Microstructure Evolution and Selective Corrosion Resistance in Underwater Multi-pass 2101 Duplex Stainless Steel Welding Joints, *Metall. Mater. Trans. A*, 2018, **49**, p 3306–3320

10. C.G.S. Leite, E.J. da Cruz Junior, M. Lago, A. Zambon, I. Calliari and V.A. Ventrella, Nd:YAG Pulsed Laser Dissimilar Welding of UNS S32750 Duplex with Austenitic Stainless Steel, *Metals*, 2019, **12**, p 2906

11. N. Ouali, K. Khenfer, B. Belkessa, J. Fajoui, B. Cheniti, B. Idir and S. Branchu, Effect of Heat Input on Microstructure, Residual Stress, and Corrosion Resistance of UNS 32101 Lean Duplex Stainless Steel Weld Joints, *J. Mater. Eng. Perform.*, 2019, **28**, p 4252–4264

12. B. Varbai and K. Májlinger, Physical and Theoretical Modelling of Nitrogen Content of Duplex Stainless Steel Weld Metal: Shielding Gas Composition and Heat Input Effects, *Metals*, 2019, **9**, p 762

13. V. Muthupandi, P. Bala Srinivasan, V. Shankar, S.K. Seshadri and S. Sundaresan, Effect of Nickel and Nitrogen Addition on the Microstructure and Mechanical Properties of Power Beam Processed Duplex Stainless Steel (UNS 31803) Weld Metals, *Mater. Lett.*, 2005, **59**, p 2305–2309

14. K. Migiakis and G.D. Papadimitriou, Effect of Nitrogen and Nickel on the Microstructure and Mechanical Properties of Plasma Welded UNS S32760 Super-Duplex Stainless Steels, *J. Mater. Sci.*, 2009, **44**, p 6372–6383

15. J. Pilhagen and R. Sandström, Influence of Nickel on the Toughness of Lean Duplex Stainless Steel Welds, *Mater. Sci. Eng. A*, 2014, **602**, p 49–57

16. A. Tahaei, A.F.M. Perez, M. Merlin, F.A.R. Valdes and G.L. Garagnani, Effect of the Addition on Nickel Powder and Post Weld Heat Treatment on the Metallurgical and Mechanical Properties of the Welded UNS S32304 Duplex, *Rev. Soldagem Inspecao*, 2016, **21**(2), p 197–208

17. Z. Zhang, H. Jing, L. Xu, Y. Han, L. Zhao and C. Zhou, Effects of Nitrogen in Shielding Gas on Microstructure Evolution and Localized Corrosion Behavior of Duplex Stainless Steel Welding Joints, *Appl. Surf. Sci.*, 2017, **404**, p 110–128

18. E.J. da Cruz Junior, O.D. Franzini, I. Calliari and V.A. Ventrella, Effects of Nickel Addition on the Microstructure of Laser-Welded UNS S32750 Duplex Stainless Steel, *Metall. Mater. Trans. A*, 2019, **50**, p 1616–1618

19. "Standard Test Methods for Tension Testing of Metallic Materials," E8 / E8M-16ae1, ASTM, 2016

20. C. Gennari, M. Lago, B. Bögre, I. Meszaros, I. Calliari and L. Pezzato, Microstructural and Corrosion Properties of Cold Rolled Laser Welded UNS S32750 Duplex Stainless Steel, *Metals*, 2018, **8**, p 1074

21. "Standard Test Method for Electrochemical Critical Pitting Temperature Testing of Stainless Steels and Related Alloys," G150-18, ASTM, 2018

22. G.R. Mohammed, M. Ishak, S.N. Aqida and H.A. Abdulhadi, Effects of Heat Input on Microstructure, Corrosion and Mechanical Characteristics of Welded Austenitic and Duplex Stainless Steel: A Review, *Metals*, 2017, **7**, p 39

23. V. Muthupandi, P. Bala Srinivasan, S.K. Seshadri and S. Sundaresan, Effect of Weld Metal Chemistry and Heat Input on the Structure and Properties of Duplex Stainless Steel Welds, *Mater. Sci. Eng. A*, 2003, **358**, p 9–16

24. R. Badjia, M. Bouabdallah, B. Bacroix, C. Kahloun, B. Belkessa and H. Maza, Phase Transformation and Mechanical Behavior in Annealed 2205 Duplex Stainless Steel Welds, *Mater. Charact.*, 2008, **59**, p 447–453

25. Z. Zhang, Z. Wang, Y. Jiang, H. Tan, D. Han, Y. Guo and J. Li, Effect of Post-Weld Heat Treatment on Microstructure Evolution and Pitting Corrosion Behavior of UNS S31803 Duplex Stainless Steel Welds, *Corros. Sci.*, 2012, **62**, p 42–50

26. Y. Yang, Z. Wang, H. Tan, J. Hong, Y. Jiang, L. Jiang and J. Li, Effect of a Brief Post-Weld Heat Treatment on the Microstructure Evolution and Pitting Corrosion of Laser Beam Welded UNS S31803 Duplex Stainless Steel, *Corros. Sci.*, 2012, **65**, p 472–480

27. J. Singh and A.S. Shahi, Metallurgical, Impact and Fatigue Performance of Electron Beam Welded Duplex Stainless Steel Joints, *J. Mater. Process. Tech.*, 2019, **272**, p 137–148

28. D.H. Kang and H.W. Lee, Study of the Correlation Between Pitting Corrosion and the Component Ratio of the Dual Phase in Duplex Stainless Steel Welds, *Corros. Sci.*, 2013, **74**, p 396–407

29. S. Saravanan, N. Sivagurumanikandan and K. Raghukandanb, Effect of Heat Input on Microstructure and Mechanical Properties of Nd: YAG Laser Welded Super Duplex Stainless Steel-Numerical and Experimental Approach, *Optik*, 2019, **185**, p 447–455